

Magic-angle Twisted Bilayer Systems with Quadratic-Band-Touching: Exactly Flat Bands with High-Chern Number

Ming-Rui Li,¹ Ai-Lei He,^{2,*} and Hong Yao^{1,3,†}

¹*Institute for Advanced Study, Tsinghua University, Beijing 100084, China*

²*College of Physics Science and Technology, Yangzhou University, Yangzhou 225002, China*

³*State Key Laboratory of Low Dimensional Quantum Physics, Tsinghua University, Beijing 100084, China*

(Dated: December 27, 2022)

Studies of twisted moiré systems have been mainly focused on two-dimensional (2D) materials such as graphene with Dirac points and transition-metal-dichalcogenide so far. Here we propose a twisted bilayer of 2D systems which feature stable quadratic-band-touching points and find exotic physics different from previously studied twisted moiré systems. Specifically, we show that exactly flat bands can emerge at magic angles and, more interestingly, *each* flat band exhibits a high Chern number ($C = \pm 2$). We further consider the effect of Coulomb interactions in such magic-angle twisted systems and find that the ground state supports the quantum anomalous Hall effect with quantized Hall conductivity $2\frac{e^2}{hc}$ at certain filling. Furthermore, the possible physical realization of such twisted bilayer systems will be briefly discussed.

Introduction: Twisted moiré systems, especially twisted bilayer graphene (TBG), have attracted enormous attention in recent years due to the emergence of topological flat bands and various interesting phases such as correlation insulators and unconventional superconductivity [1–26]. Since its experimental discovery, extensive studies of such systems have been done on both experimental and theoretical sides. The theoretical prediction of flat bands in TBG was made by Bistritzer and MacDonald (BM) [27], in their paper the BM Hamiltonian and the moiré band theory were developed to study TBG and other twisted moiré systems. Furthermore, a generalization of the BM model was developed [28] and a more complete description and understanding of the flat bands in a twisted bilayer system were obtained through perturbation theory. Based on the moiré band theory, enormous numbers of studies were done to explore the topological features [29–32] as well as the interaction effects [33–80] of TBG systems; non-trivial topology of the flat bands has been shown, and huge progress has been made in understanding the interacting phases.

Although twisted systems have attracted vast research attention, studies of them have been mainly limited to twisted graphene systems with Dirac fermions and twisted transition-metal-dichalcogenide (TMD) [81–96]; explorations of twisted systems with other types of fermions, such as those with quadratic band touchings, remain scarce. It is desired to study such new types of twisted systems mainly for the following reasons. On the one hand, the larger density of states in these systems may lead to nontrivial interacting phases [97–100]. On the other hand, the possibility of realizing higher-Chern number flat bands in such twisted systems is attractive as high-Chern-number flat bands can provide an arena to realize various exotic fractional quantum Hall effects [101–109] and its realization in quantum materials remains elusive.

In this paper, we investigate a twisted bilayer of

systems with quadratic band touching, with focus on the twisted bilayer checkerboard (TBCB) model. The checkerboard lattice model in each single layer was proposed by Sun, Yao, Fradkin, and Kivelson (SYFK) [97] to realize a stable quadratic band touching point (QBTP). Note that for *AB*-bilayer graphene, the putative QBTP is not stable in the presence of trigonal hopping [110]. We found that such twisted systems can host two exactly flat bands per spin in the chiral limit, and more interestingly, *each* flat band has nontrivial topology with high Chern number $C = \pm 2$. Note that, in contrast to TBG with a total of eight flat bands, there are only four flat bands in the TBCB. In the presence of Coulomb interactions, by projecting them onto the topological flat bands of $C = \pm 2$ in TBCB systems similar to the analysis employed for TBG [72, 73], we showed that the interaction prefers the ground state with minimum Chern number; at charge-neutrality ($\nu = 0$) the ground state is an insulator with Chern number $C = 0$, while for $\nu = \pm 1$ the ground state possesses Chern number ± 2 and exhibits the quantum anomalous Hall effect [5, 7, 16, 111]. We further propose a possible optical-lattice realization of the TBCB with topological flat bands, providing a promis-

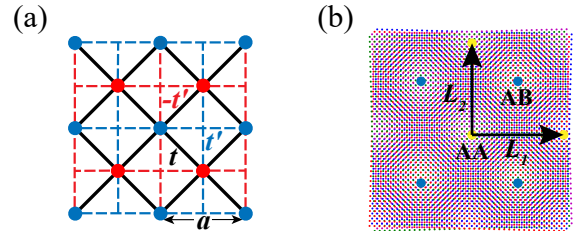


FIG. 1. (a) Schematic representation of the checkerboard lattice. Blue and red sites constitute sublattices *A* and *B*, respectively. Note that the intra-sublattice hopping in sublattice *A* is opposite to that in sublattice *B*. (b) The moiré pattern of the TBCB lattice.

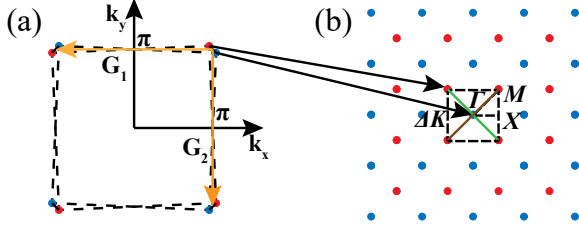


FIG. 2. (a) The Brillouin zone of the top (blue) and bottom (red) layer. \mathbf{G}_1 and \mathbf{G}_2 is plotted in yellow. (b) The moiré Brillouin zone of the TBCB lattice. The blue points represent the \mathbf{M} points of the top layer while the red points represent the \mathbf{M} points of the bottom layer. We pick the square surrounded by dashed lines as our mBZ, and label the three high-symmetry points as Γ , X , and M .

ing route to study various correlated phases in TBCB experimentally.

Quadratic-band-touching model: One prototype model hosting stable quadratic-band-touching points (QBTPs) is the checkerboard model proposed by SYFK [97]. As shown in Fig. 1(a), it can be described by the tight-binding Hamiltonian: $H = -\sum_{i,j} t_{ij} c_i^\dagger c_j$, with the hopping amplitude t_{ij} between sites i and j . Here we consider nearest-neighbor hopping t and next-nearest-neighbor hopping $\pm t'$, as shown in Fig. 1(a). Note that the lattice consists of two sublattices labeled as A and B . By performing the Fourier transformation $c_{i \in A(B)} = \frac{1}{\sqrt{N}} \sum_{\mathbf{k}} e^{i\mathbf{k} \cdot \mathbf{r}_i} \psi_{\mathbf{k}, A(B)}$, where N is the number of unit cells, we obtain $H_0 = \sum_{\mathbf{k}} \psi^\dagger(\mathbf{k}) H_0(\mathbf{k}) \psi(\mathbf{k})$ with $\psi^\dagger = (\psi_A^\dagger, \psi_B^\dagger)$. $H_0(\mathbf{k})$ is the two-band Bloch Hamiltonian: $H_0(\mathbf{k}) = d_x(\mathbf{k})\sigma_x + d_z(\mathbf{k})\sigma_z$, where $d_z(\mathbf{k}) = -4t \cos(k_x/2) \cos(k_y/2)$ and $d_x(\mathbf{k}) = 2t'(\cos k_x - \cos k_y)$ [112]. It is straightforward to obtain the dispersion of two bands: $\epsilon_{\mathbf{k}, \pm} = \pm \sqrt{d_x^2(\mathbf{k}) + d_z^2(\mathbf{k})}$. By expanding the periodic Bloch Hamiltonian around $\mathbf{M} = (\pi, \pi)$ where two bands cross (namely $\mathbf{k} \rightarrow \mathbf{k} + \mathbf{M}$) and keeping only the lowest orders in \mathbf{k} , we obtain

$$H_0(\mathbf{k}) = tk_x k_y \sigma_x + t'(k_x^2 - k_y^2) \sigma_z. \quad (1)$$

The dispersion around \mathbf{M} is quadratic and \mathbf{M} is called the quadratic-band-touching point (QBTP). To transform the Hamiltonian into a form with explicit chiral symmetry, we can perform a basis transformation $\psi \rightarrow U\psi$ with $U = e^{i\frac{\pi}{2}\sigma^x}$ and obtain $\tilde{H}_0(\mathbf{k}) = U^\dagger H_0(\mathbf{k}) U$ as

$$\tilde{H}_0(\mathbf{k}) = tk_x k_y \sigma_x + t'(k_x^2 - k_y^2) \sigma_y. \quad (2)$$

Note that the QBTP features a Berry phase of 2π , which is twice of that of a Dirac point. Hereafter, unless stated otherwise, we shall assume $t' = t/2$, so that the dispersion $E_\pm(\mathbf{k}) = \pm \frac{t}{2} \mathbf{k}^2$.

Exactly flat bands at magic angles: It is desirable to investigate novel physics in a twisted bilayer of

systems with quadratic-band-touching fermions for the exotic property of the QBTP [97]. In this paper, we consider the twisted bilayer of the checkerboard lattice, and explore its physics such as totally flat bands at magic angles and the high Chern number of those flat bands. The lattice structure of the TBCB lattice is shown in Fig. 1(b).

Here we mainly focus on the low-energy physics of the twisted bilayer system with quadratic band touching by employing the continuum model describing the low-energy band structure around the QBTP \mathbf{M} . Using the moiré band theory introduced by Bistritzer and MacDonald [27], we obtained the inter-layer hopping matrices: $T_{\mathbf{p}\mathbf{p}'}^{\alpha\beta} = \sum_{\mathbf{G}_1, \mathbf{G}_2} \frac{t_{\mathbf{p}+\mathbf{G}_1}}{\Omega} e^{i\mathbf{G}_1 \cdot \tau_\alpha - i\mathbf{G}_2 \cdot \tau_\beta} \delta_{\mathbf{p}+\mathbf{G}_1, \mathbf{p}'+\mathbf{M}_\theta \mathbf{G}_2}$, where $\mathbf{G}_1, \mathbf{G}_2$ are the reciprocal vectors of the lattice, α and β labels the sublattice indices A and B , respectively, M_θ represents the rotation by angle θ , and $\tau_{\alpha(\beta)}$ represents the relative coordinates of the sublattice $\alpha(\beta)$ in the unit cell. For the checkerboard lattice shown in Fig. 1(a), we have $\tau_A = (0, 0)$ and $\tau_B = (\frac{1}{2}, \frac{1}{2})$ in the unit of lattice constant a . Inspired by the TBG theory, we only keep the largest four $t_{\mathbf{p}}$ terms, i.e., the terms with $\mathbf{p} - \mathbf{p}' = C_{4z}^i (M_\theta - 1) \mathbf{M}$, where $i = 0, 1, 2, 3$. With these four hoppings we can construct the moiré Brillouin zone (mBZ) as shown in Fig. 2(b) and the hopping matrices take the form:

$$T_1 = \begin{pmatrix} w_{AA} & w_{AB} \\ w_{AB} & w_{AA} \end{pmatrix}, \quad T_2 = \begin{pmatrix} w_{AA} & -w_{AB} \\ -w_{AB} & w_{AA} \end{pmatrix}, \quad (3)$$

where $T_1(T_2)$ is the hopping matrix of hopping along the green (brown) lines in the mBZ as shown in Fig. 2(b) [113].

Assuming the chiral limits $w_{AA} = 0$ and $w_{AB} = w$ [114], we numerically computed the moiré bands and observed exactly flat bands for a series of magic angles as shown in Fig. 3. The band structure is controlled by a single parameter $\alpha = \frac{w}{t'k_\theta^2} = \frac{wa^2}{8t'\pi^2 \sin^2(\theta/2)}$ which is proportional to $1/\sin^2(\theta/2)$. Note that the parameter α is qualitatively different from its counterpart $\frac{w}{\sin(\theta/2)}$ for TBG [114]. As a consequence, the magic angle for the TBCB can be much larger compared with TBG. This property makes the twist angle of the TBCB system easier to be tuned experimentally.

Origin of the exactly flat bands: We now provide an analytical understanding of the origin of exactly flat bands at those magic angles. First, we perform the Fourier transformation and obtain the hopping matrices in real space $T(\mathbf{r}) = \sum_{n=1}^2 2T_n \cos(\mathbf{q}_n \cdot \mathbf{r})$, where $\mathbf{q}_1 = \frac{k_\theta}{\sqrt{2}}(1, 1)$ and $\mathbf{q}_2 = \frac{k_\theta}{\sqrt{2}}(1, -1)$ with $k_\theta = \frac{2\sqrt{2}\pi}{a} \sin \frac{\theta}{2}$. Since the system preserves the chiral symmetry when $w_{AA} = 0$, we choose the basis $\Phi(\mathbf{r}) = (\psi_{1,A}, \psi_{2,A}, \psi_{1,B}, \psi_{2,B})^T$, where 1 and 2 are the layer indices and A and B are the sublattice indices, such that the Hamiltonian is given

by

$$H(\mathbf{r}) = \begin{pmatrix} 0 & \mathcal{D}(\mathbf{r}) \\ \mathcal{D}^*(-\mathbf{r}) & 0 \end{pmatrix}, \quad (4)$$

where $\mathcal{D}(\mathbf{r})$ is completely antiholomorphic:

$$\mathcal{D}(\mathbf{r}) = \begin{pmatrix} -i\frac{t}{2}\bar{\partial}^2 & 2w[\cos(\mathbf{q}_1 \cdot \mathbf{r}) - \cos(\mathbf{q}_2 \cdot \mathbf{r})] \\ 2w[\cos(\mathbf{q}_1 \cdot \mathbf{r}) - \cos(\mathbf{q}_2 \cdot \mathbf{r})] & -i\frac{t}{2}\bar{\partial}^2 \end{pmatrix}, \quad (5)$$

with $\bar{\partial} \equiv \partial_{\bar{z}} = \partial_x - i\partial_y$ [hereinafter we shall use $\mathbf{r} = (x, y)$ and $z = x + iy$ interchangeably].

The QBTP at \mathbf{M} with zero energy is protected by symmetry. Explicitly, the zero-energy wave function $\phi_{\mathbf{M}}$ satisfying $H\phi_{\mathbf{M}} = 0$ is given by $\phi_{\mathbf{M}}^T = (0, 0, \psi_{\mathbf{M}}^T)$, where $\psi_{\mathbf{M}}(\mathbf{r})$ is a two-component wavefunction satisfying $\mathcal{D}\psi_{\mathbf{M}}(\mathbf{r}) = 0$. Since \mathcal{D} is antiholomorphic, we can construct the wavefunction $\psi_{\mathbf{k}}(\mathbf{r}) = f_{\mathbf{k}}(z)\psi_{\mathbf{M}}(\mathbf{r})$, where $f_{\mathbf{k}}(z)$ is a holomorphic function, with the following feature: $\mathcal{D}\psi_{\mathbf{k}}(\mathbf{r}) = f_{\mathbf{k}}(z)\mathcal{D}\psi_{\mathbf{M}}(\mathbf{r}) = 0$. If such a holomorphic function $f_{\mathbf{k}}(z)$ exists for every \mathbf{k} in the mBZ, the wavefunction of the totally flat band with momentum \mathbf{k} is obtained. Note that $\psi_{\mathbf{M}}$ satisfy the Moire boundary condition $\psi_{\mathbf{M}}(z + L_j) = \sigma_z \psi_{\mathbf{M}}(z)$ which means $f_{\mathbf{k}}(z + L_j) = e^{i\mathbf{k} \cdot \mathbf{L}_j} f_{\mathbf{k}}(z)$, where $L_j = \mathbf{L}_j \cdot \hat{x} + i\mathbf{L}_j \cdot \hat{y}$ [114]; consequently, $f_{\mathbf{k}}(z)$ must have a simple pole, and such a construction fails in general. However, when $\psi_{\mathbf{M}}(\mathbf{r})$ has a zero point at special twist angles, nonsingular $f_{\mathbf{k}}(z)$ is permitted, and the exactly flat bands from the construction above can exist. Such a special twist angle at which $\psi_{\mathbf{M}}(\mathbf{r})$ has zeros is a so-called magic angle. Indeed, our calculation of $\psi_{\mathbf{M}}$ with zero energy at the magic angle shows that $\psi_{\mathbf{M}}(\mathbf{r})$ is zero when \mathbf{r} is at AA stacking point, as shown in Fig. 3(f).

Derivation of the first magic angle: Based on the requirement that at the magic angle the wave function $\phi_{\mathbf{M}}(\mathbf{r}) = 0$ for \mathbf{r} at the AA stacking point, we can analytically derive the parameter α corresponding to the magic angle. Solving the equation $\mathcal{D}\psi_{\mathbf{M}}(\mathbf{r}) = 0$ perturbatively in the parameter $\alpha < 1$, we obtain the spinor wave function

$$\psi_{\mathbf{M}}(\mathbf{r}) = (1 + u_1\alpha + u_2\alpha^2 + \dots) \frac{1}{\sqrt{2}} \begin{pmatrix} 1 \\ \pm 1 \end{pmatrix}, \quad (6)$$

where \dots represents higher-order terms in α and $u_j(\mathbf{r})$ carries momentum $m\mathbf{q}_1 + n\mathbf{q}_2$ with $|m| + |n| = j$. Up to the second order u_2 , one can get the solution $u_1(\mathbf{r}) = \mp 2\alpha [\cos(\mathbf{q}_1 \cdot \mathbf{r}) + \cos(\mathbf{q}_2 \cdot \mathbf{r})]$ and $u_2(\mathbf{r}) = \frac{1}{2}\alpha^2 [\cos(2\mathbf{q}_1 \cdot \mathbf{r}) + \cos(2\mathbf{q}_2 \cdot \mathbf{r})]$. Requiring that the wavefunction is zero at the AA stacking point, namely $\psi_{\mathbf{M}}(\mathbf{0}) = (0, 0)^T$, we obtain the first magic angle solution $\alpha = \alpha_0 = 2 - \sqrt{3} \approx 0.268$, which is very close to the numerically-obtained first magic angle shown in Fig. 3(a).

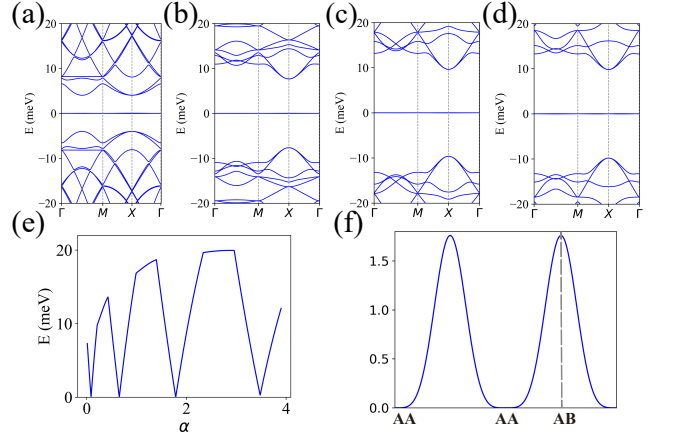


FIG. 3. (a)-(d) The band structure of the TBCB lattice with $\alpha = 0.26, 2.16, 5.93,$ and 11.62 , respectively. For each case, there exist two degenerate and totally flat bands in the middle. (e) The bandwidth of the middle two bands. The bandwidth drops to exactly zero at the magic angles. (f) The wavefunction density for a single zero mode at QBTP \mathbf{M} along the line AA-AB, a zero point exists at the AA stacking point.

Another (probably more intuitive) way to derive the magic angle is to require the vanishing of the inverse effective mass of the fermions at the QBTP \mathbf{M} which is qualitatively different from the TBG system, which only requires the vanishing of the Fermi velocity at magic angles. Requiring the vanishing of the inverse effective mass of the fermions at the QBTP \mathbf{M} , we obtain the first magic-angle parameter $\alpha = \frac{1}{\sqrt{12}} \approx 0.289$, which is also quite close to the value obtained numerically in Fig. 3(a). Details of computing the inverse effective mass are shown in Appendix B.

High-Chern number of exactly flat bands: To analyze the topology of these flat bands, we first calculate the Wilson loop's winding number of the TBCB lattice. For the Bloch states in the moiré Brillouin zone, to define the Wilson loop, we need to first restore the periodicity of the Bloch states and thus need to introduce the extra embedding matrix $V_{\mathbf{Q}, \mathbf{Q}'}^{\mathbf{G}} = \delta_{\mathbf{Q}-\mathbf{G}, \mathbf{Q}'}$. Consequently, the Wilson loop for the TBCB lattice is calculated by

$$W(k_1) = U_{k_1, 0}^\dagger U_{k_1, \frac{2\pi}{N}} \cdots U_{k_1, \frac{(N-1) \times 2\pi}{N}}^\dagger V^{\mathbf{G}} U_{k_1, 0}. \quad (7)$$

where $U_{k_1, k_2} = U_{\mathbf{k}} = (|u_{1\mathbf{k}}\rangle, \dots, |u_{N\mathbf{k}}\rangle)$ with $\mathbf{k} = (k_1, k_2)$ [29, 32, 115]. We assume that \mathbf{b}_1 and \mathbf{b}_2 are the reciprocal vectors of the moiré lattice, $\mathbf{k} = k_1\mathbf{b}_1 + k_2\mathbf{b}_2$. We keep k_1 unchanged and vary k_2 to obtain the flow of the Wilson loop spectrum along k_1 . We find that the Wilson loop winds from ± 1 to ∓ 1 twice while k_1 goes from $-\pi$ to π , so the winding of the Wilson loop at the first magic angle is ± 2 , as shown in the Fig. 4. This is also true for other magic angles that we identified. When adding more bands into the Wilson loop calculation such as the middle six bands, the winding is still preserved which

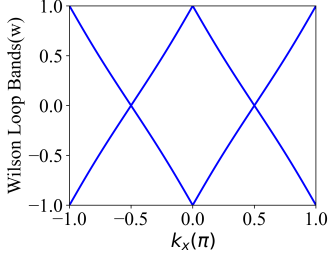


FIG. 4. Wilson-loop bands of the flat bands at the first magic angle $\alpha = 0.26$. The two Wilson loops wind from ± 1 to ∓ 1 twice as k_1 varies from $-\pi$ to π . Thus the winding number of the Wilson loop is ± 2 .

suggests that the topology is stable. In fact, the anti-unitary particle-hole symmetry P (see the Appendix C) protects the degeneracy of the Wilson bands at $k_1 = 0/\pi$ in the same way as in TBG [32].

In the non-interacting limit, the degeneracy of the two flat bands for the TBCB is protected by the time-reversal symmetry T . To give a simple illustration of the topology with the existence of interactions, we apply a weak time-reversal-symmetry-breaking term which preserves all other symmetries except the mirror symmetry: $A\sigma_y \sin(\frac{k_x}{2}) \sin(\frac{k_y}{2})$. The degeneracy is then lifted, while the flatness of bands is still well preserved. Assuming $A/w_{AB} = 0.5$, we have calculated the Berry curvature of the two flat bands and the corresponding Chern number: $C_n = \frac{1}{2\pi} \int_{\text{mBZ}} \mathcal{B}_n d k_x d k_y$. Our result shows that the lower band hosts a Chern number of ∓ 2 , while the upper band host a Chern number of ± 2 where the sign of the Chern number depends on the sign of A . For a spinless TBCB system, this is the only possible way for the two bands to split; the topology of the system is highly nontrivial with high Chern number $C = \pm 2$. It is noteworthy that this high Chern number of ± 2 is realized in the flat bands of a twisted bilayer systems [116] with stable QBTPs, and in our system, the QBTPs have only one valley, which will lead to different physics.

Correlation effect: Interactions can play an essential role in the physics of twisted bilayer systems [33–40, 42–47, 49–79]. Here, we consider the Coulomb interactions:

$$\mathcal{H}_I = \frac{1}{2A} \sum_{\mathbf{G} \in \mathcal{G}, \mathbf{q} \in \text{mBZ}} V(\mathbf{q} + \mathbf{G}) \delta \rho_{-\mathbf{q}-\mathbf{G}} \delta \rho_{\mathbf{q}+\mathbf{G}}, \quad (8)$$

where $\delta \rho_{\mathbf{q}} = \sum_{\mathbf{r}} e^{i\mathbf{q} \cdot \mathbf{r}} (\rho_{\mathbf{r}} - \frac{1}{2} \delta_{\mathbf{q},0} \delta_{\mathbf{G},0})$, \mathcal{G} represents the moiré reciprocal lattice vectors in the Brillouin zone (BZ) of the original lattice, and $V(\mathbf{q}) = \pi d^2 U_d \frac{\tanh(d|\mathbf{q}|/2)}{d|\mathbf{q}|/2}$ is the screened Coulomb potential with $U_d = e^2/(\epsilon d)$ [72]; d is the distance between the TBG and the top or bottom gate, and $\rho_{\mathbf{r}}$ is the charge density at \mathbf{r} . To solve its low-energy physics, one can project the Hamiltonian onto the subspace of the two flat bands. To

do so, we employ fermion operators in the mBZ energy band basis $c_{n,s}^\dagger(\mathbf{k}) = \sum_{\mathbf{Q} \in \mathcal{Q}_\pm} u_{\mathbf{Q},\alpha,n}(\mathbf{k}) f_{\alpha,s}^\dagger(\mathbf{k} + \mathbf{Q})$, where $\mathbf{Q} \in \mathcal{Q}_\pm$ and \mathcal{Q}_\pm is the collection of the sites of layer $l = \pm$ of the mBZ as plotted in Fig. 2. Here, n is the moiré band index, and $n = \pm 1$ represents the two flat bands. Due to its nontrivial topology, we cannot define a symmetric smooth and periodic wave function $u_{\mathbf{Q},\alpha,n}(\mathbf{k})$ [68]. Here we adopt a periodic gauge that satisfies $u_{\mathbf{Q},\alpha,n}(\mathbf{k} + \mathbf{b}_i) = u_{\mathbf{Q}-\mathbf{G},\alpha,n}(\mathbf{k})$. Similar to the treatment of interactions in TBG [72, 73], after the projection into the flat band subspace the interacting Hamiltonian for the TBCB system is written as

$$H_I = \frac{1}{2\Omega_{\text{tot}}} \sum_{\mathbf{q} \in \text{mBZ}} \sum_{\mathbf{G} \in \mathcal{G}} O_{-\mathbf{q},-\mathbf{G}} O_{\mathbf{q},\mathbf{G}}, \quad (9)$$

where Ω_{tot} is the total area of the TBCB system,

$$O_{\mathbf{q},\mathbf{G}} = \sum_{\mathbf{k},s} \sum_{m,n=\pm 1} \sqrt{V(\mathbf{q}+\mathbf{G})} M_{m,n}(\mathbf{k}, \mathbf{q}+\mathbf{G}) \times \left(c_{m,s}^\dagger(\mathbf{k}+\mathbf{q}) c_{n,s}(\mathbf{k}) - \frac{1}{2} \delta_{\mathbf{q},0} \delta_{m,n} \right), \quad (10)$$

and

$$M_{mn}(\mathbf{k}, \mathbf{q}+\mathbf{G}) = \sum_{\alpha, \mathbf{Q} \in \mathcal{Q}_\pm} u_{\mathbf{Q}-\mathbf{G},\alpha,m}^*(\mathbf{k}+\mathbf{q}) u_{\mathbf{Q},\alpha,n}(\mathbf{k}). \quad (11)$$

As discussed in the Appendix C, considering the C_{2z} , T , and P symmetries, the M matrix is constrained as follows:

$$M(\mathbf{k}, \mathbf{q}+\mathbf{G}) = \zeta^0 \alpha_0(\mathbf{k}, \mathbf{q}+\mathbf{G}) + i\zeta^y \alpha_2(\mathbf{k}, \mathbf{q}+\mathbf{G}), \quad (12)$$

where ζ represents the Pauli matrix for the two-flat-band subspace, $\alpha_0(\mathbf{k}, \mathbf{q}+\mathbf{G})$ and $\alpha_2(\mathbf{k}, \mathbf{q}+\mathbf{G})$ are real numbers with the constraints $\alpha_0(\mathbf{k}, \mathbf{q}+\mathbf{G}) = \alpha_0(\mathbf{k}+\mathbf{q}, -\mathbf{q}-\mathbf{G})$ and $\alpha_2(\mathbf{k}, \mathbf{q}+\mathbf{G}) = -\alpha_2(\mathbf{k}+\mathbf{q}, -\mathbf{q}-\mathbf{G})$ and $\alpha_a(\mathbf{k}, \mathbf{q}+\mathbf{G}) = \alpha_a(-\mathbf{k}, -\mathbf{q}-\mathbf{G})$ for $a = 0, 2$ (see details in the Appendix C).

In the Chern band basis [32, 72] which is the eigenstate of the flat bands with Chern number $C = 2e$: $d_{\mathbf{k},e,s}^\dagger = \frac{c_{1,s}^\dagger(\mathbf{k}) + iec_{-1,s}^\dagger(\mathbf{k})}{\sqrt{2}}$, where $e = \pm 1$, we can rewrite the operator $O_{\mathbf{q},\mathbf{G}}$ in a diagonal way

$$O_{\mathbf{q},\mathbf{G}} = \sum_{\mathbf{k},s} \sum_{e=\pm 1} \sqrt{V(\mathbf{q}+\mathbf{G})} M_e(\mathbf{k}, \mathbf{q}+\mathbf{G}) \times \left(d_{\mathbf{k}+\mathbf{q},e,s}^\dagger d_{\mathbf{k},e,s} - \frac{1}{2} \delta_{\mathbf{q},0} \right), \quad (13)$$

where $M_e(\mathbf{k}, \mathbf{q}+\mathbf{G}) = \alpha_0(\mathbf{k}, \mathbf{q}+\mathbf{G}) + iec_2(\mathbf{k}, \mathbf{q}+\mathbf{G})$. Following the Lagrange multiplier method introduced in Refs. [72, 73], the ground state satisfies the equation $(O_{\mathbf{q},\mathbf{G}} - A_{\mathbf{G}} N \delta_{\mathbf{q},0}) |\Psi\rangle = 0$, where N is the total number of electrons and $A_{\mathbf{G}}$ is the multiplier (see details in Appendix D). Assuming an integer filling ν and $A_{\mathbf{G}} = \frac{\nu}{N} \sqrt{V(\mathbf{G})} \sum_{\mathbf{k}} \alpha_0(\mathbf{k}, \mathbf{G})$, the ground states take the form $|\Psi_{\nu^+, \nu^-}\rangle = \prod_{\mathbf{k}} \prod_{j_1=1}^{\nu^+} d_{\mathbf{k}+1, s_{j_1}}^\dagger \prod_{j_2=1}^{\nu^-} d_{\mathbf{k}-1, s_{j_2}}^\dagger |0\rangle$, where

$\nu + 2 = \nu_+ + \nu_-$ is the total filling factor of the system with ν_{\pm} being the integer filling of the Chern bands with Chern number $C = \pm 2$. It is clear that the state $|\Psi_{\nu^+, \nu^-}\rangle$ carries a Chern number of $2(\nu_+ - \nu_-)$ and different states with the same ν are degenerate.

In real TBCB systems, it is difficult to tune the intrasublattice hopping w_{AA} to be strictly zero. When $w_{AA} \neq 0$, neither the particle-hole symmetry nor the chiral symmetry holds (see Appendix C for details). Thus the M matrix takes a general form

$$M(\mathbf{k}, \mathbf{q} + \mathbf{G}) = \zeta^0 \alpha_0(\mathbf{k}, \mathbf{q} + \mathbf{G}) + \zeta^x \alpha_1(\mathbf{k}, \mathbf{q} + \mathbf{G}) + i\zeta^y \alpha_2(\mathbf{k}, \mathbf{q} + \mathbf{G}) + \zeta^z \alpha_3(\mathbf{k}, \mathbf{q} + \mathbf{G}). \quad (14)$$

In the Chern basis, the operator $O_{\mathbf{q}, \mathbf{G}} = O_{\mathbf{q}, \mathbf{G}}^0 + O_{\mathbf{q}, \mathbf{G}}^1$ where $O_{\mathbf{q}, \mathbf{G}}^0$ is given by Eq. (13), while $O_{\mathbf{q}, \mathbf{G}}^1$ reads

$$O_{\mathbf{q}, \mathbf{G}}^1 = \sum_{\mathbf{k}, s, e = \pm 1} \sqrt{V(\mathbf{q} + \mathbf{G})} F_e(\mathbf{k}, \mathbf{q} + \mathbf{G}) d_{\mathbf{k} + \mathbf{q}, -e, s}^\dagger d_{\mathbf{k}, e, s}, \quad (15)$$

where $F_e(\mathbf{k}, \mathbf{q} + \mathbf{G}) = ie\alpha_1(\mathbf{k}, \mathbf{q} + \mathbf{G}) + \alpha_3(\mathbf{k}, \mathbf{q} + \mathbf{G})$. When the system has an even filling factor ν and assuming the flat band approximation, the ground state of the operator $O_{\mathbf{q}, \mathbf{G}}^1$ becomes $|\Psi_\nu\rangle = \prod_{\mathbf{k}} \prod_{j=1}^{(\nu+2)/2} d_{\mathbf{k}, +1, s_j}^\dagger d_{\mathbf{k}, -1, s_j}^\dagger |0\rangle$, which has a zero Chern number. For odd filling factors ν , after taking $O_{\mathbf{q}, \mathbf{G}}^1$ as a perturbation, the degeneracy of the different Chern states will be lifted, and $O_{\mathbf{q}, \mathbf{G}}^1$ prefers the ground state with minimum Chern number. For instance, when $\nu = \pm 1$, the system possesses a ground state with broken time-reversal symmetry and high Chern number $C = \pm 2$.

Discussions and concluding remarks: In this paper, we proposed a twisted bilayer system of fermions with C_4 -symmetry-protected quadratic band touching, which can exhibit exactly flat bands with high Chern numbers $C = \pm 2$. Our system's symmetry and the *stable* QBTPs are noteworthy aspects of this study of the twisted graphene system. The origin of the exactly flat band is related to the anti-holomorphic property of the Hamiltonian in the chiral limit with $t \neq 2t'$. At the first magic angle, the flatness of the topological bands is rather robust against deviation from the exactly flat conditions; that is, the topological bands in the middle exhibiting a high Chern number of ± 2 are nearly flat for a wide range of parameters. See details in the Appendix A.

Such a TBCB lattice may be realized by loading cold atoms into a specially-designed optical-lattice system [117, 118]. It has been proposed that the twisted square lattice can be realized by introducing four states (labeled by spin $\pm 1/2$ and two layers) and constraining each "layer" by a set of square optical lattices that differ by polarization and a small twisting angle [119]. If 2π fluxes are added to the square plaquettes such that the hopping amplitude along its diagonal is $-t'$, the TBCB lattice maybe experimentally realized, and the quantum anomalous Hall effect associated with the flat band with

high Chern number may be observed. Furthermore, away from integer filling, it is also possible to realize interesting phases such as unconventional superconductivity and fractional Chern insulators, which are left for future studies.

Acknowledgments: We would like to thank Andrei Bernevig, Eduardo Fradkin, Steve Kivelson, Kai Sun, and Zhi-Da Song for their helpful discussions. This work was supported in part by the MOSTC under Grant No. 2018YFA0305604 (H.Y.), the NSFC under Grants No. 11825404 (M.-R.L., A.-L.H., and H.Y.) and No. 12204404 (A.-L.H.), and the CAS Strategic Priority Research Program under Grant No. XDB28000000 (H.Y.).

Appendix A. Robustness of the Flat Bands

As discussed in the main text, the exactly flat band criteria of the TBCB require $t = 2t'$ and $w_{AA} = 0$. In this appendix, we show how the flatness of the two flat bands is affected by these two parameters near the first magic angle. We calculated the bandwidth of the middle two flat bands while varying t or w_{AA} . The results are shown in Fig. S1. Notice that if $w_{AA} \neq 0$, the particle-hole symmetry is broken, and thus the flat bands deviate from zero energy.

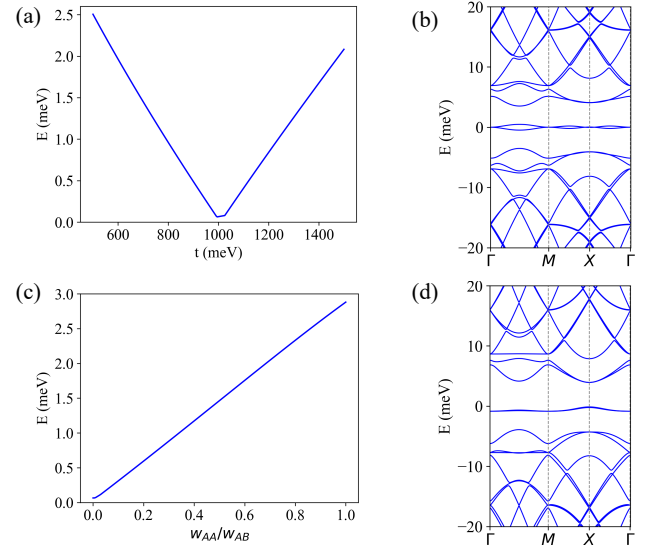


FIG. S1. (a) The bandwidth of the middle two flat bands while varying t from 500 to 1500 meV. (b) The band structure with $t' = 500$ meV, $t = 800$ meV, $w_{AA} = 0.0$ meV, $w_{AB} = 2.05$ meV, and $\theta = 1.6^\circ$. (c) The bandwidth of the middle two flat bands while varying w_{AA} from 0 to 2.0 meV. (d) The band structure with $t' = 500$ meV, $t = 1000$ meV, $w_{AA} = 0.5$ meV, $w_{AB} = 2.05$ meV, and $\theta = 1.6^\circ$.

As shown in Fig. S1(a), as t varies from 500 meV to 1500 meV, the bandwidth of the flat bands varies from 0 to 2.5 meV which is relatively small. As w_{AA} varies

from 0 to 2.0 meV [Fig. S1(c)], the bandwidth of the flat bands varies from 0 to 3 meV. The flat bands are quite robust against the deviation of the parameters.

Appendix B. Another Derivation of the First Magic Angle

We now provide another derivation of the first magic angle by requiring the vanishing of the inverse effective mass of the fermions at the QBTP. (Note that this is in contrast to the magic-angle definition of vanishing Fermi velocity in TBG.) Here we only consider the nearest four M points of the bottom layer (red) to the center point of the top layer (blue) in the mBZ, as shown in Fig. 2 of the main text. We write the ten-band Hamiltonian in the momentum space for these five points in the mBZ:

$$\mathcal{H}(\mathbf{k}) = \begin{pmatrix} \mathcal{H}_0(\mathbf{0}) & \mathcal{T}_1 & \mathcal{T}_2 & \mathcal{T}_3 & \mathcal{T}_4 \\ \mathcal{T}_1 & \mathcal{H}_0(\mathbf{q}_1) & 0 & 0 & 0 \\ \mathcal{T}_2 & 0 & \mathcal{H}_0(\mathbf{q}_2) & 0 & 0 \\ \mathcal{T}_3 & 0 & 0 & \mathcal{H}_0(\mathbf{q}_3) & 0 \\ \mathcal{T}_4 & 0 & 0 & 0 & \mathcal{H}_0(\mathbf{q}_4) \end{pmatrix}, \quad (\text{S1})$$

where $\mathcal{H}_0(\mathbf{q}) = \begin{pmatrix} 0 & -it'(\bar{\mathbf{k}} - \bar{\mathbf{q}})^2 \\ -it'(\mathbf{k} - \mathbf{q})^2 & 0 \end{pmatrix}$, $\mathcal{T}_1 = \mathcal{T}_3 = T_1$, and $\mathcal{T}_2 = \mathcal{T}_4 = T_2$. The wavefunction $(\psi_t, \psi_{b,1}, \psi_{b,2}, \psi_{b,3}, \psi_{b,4})$ satisfies the Schrödinger equation:

$$\mathcal{H}_0(\mathbf{0})\psi_t + \sum_i \mathcal{T}_i \psi_{b,i} = E\psi_t, \quad (\text{S2a})$$

$$\mathcal{T}_i \psi_t + \mathcal{H}_0(\mathbf{q}_i) \psi_{b,i} = E\psi_{b,i}, \quad i = 1, 2, 3, 4. \quad (\text{S2b})$$

From Eq. (S2b) we obtain that $\psi_{b,i} = (E - \mathcal{H}_0(\mathbf{q}_i))^{-1} \mathcal{T}_i \psi_t$, from which we can get the effective Schrödinger equation for ψ_t :

$$\left[\mathcal{H}_0(\mathbf{0}) + \sum_i \frac{\mathcal{T}_i (E + \mathcal{H}_0(\mathbf{q}_i)) \mathcal{T}_i}{E^2 - t'^2 (k^2 + q_i^2 - 2\vec{k} \cdot \vec{q}_i)^2} \right] \psi_t = E\psi_t. \quad (\text{S3})$$

Neglecting the E^2 and k^n for $n > 2$ terms as small and noticing that $q_i^2 = 1$, we get

$$\frac{\mathcal{H}_0(\mathbf{0}) - \sum_i \frac{\mathcal{T}_i \mathcal{H}_0(\mathbf{q}_i) \mathcal{T}_i}{t'^2 (1 + k^2 - 2\vec{k} \cdot \vec{q}_i)^2}}{1 + \sum_i \frac{w^2}{t'^2 (1 + k^2 - 2\vec{k} \cdot \vec{q}_i)^2}} \psi_t = E\psi_t. \quad (\text{S4})$$

Substituting the \mathcal{T}_i we have obtained before, one can get the effective Hamiltonian

$$\mathcal{H} = \begin{pmatrix} 0 & -it_{\text{eff}} \bar{\mathbf{k}}^2 \\ -it_{\text{eff}} \mathbf{k}^2 & 0 \end{pmatrix}, \quad (\text{S5})$$

with $t_{\text{eff}} = \frac{1-12\alpha^2}{1+4\alpha^2} t'$. When $\alpha = \frac{1}{\sqrt{12}} \approx 0.289$, $t_{\text{eff}} \propto m_{\text{eff}}^{-1}$ tends to zero and flat bands emerge. This result is close to the first magic angle we obtained numerically.

Appendix C. Symmetries of the Twisted Bilayer Checkerboard Lattice and Gauge fixing

The Hamiltonian of the twisted bilayer checkerboard lattice is

$$H = \sum_l \sum_{\mathbf{k}} f_{l,\mathbf{k}}^\dagger h_{l\theta/2}(\mathbf{k}) f_{l,\mathbf{k}} + \sum_{\mathbf{k}} \sum_{i=1}^2 \left(f_{1,\mathbf{k}}^\dagger T_i f_{-1,\mathbf{k}+\mathbf{q}_i} + f_{1,\mathbf{k}}^\dagger T_i f_{-1,\mathbf{k}-\mathbf{q}_i} + \text{H.c.} \right), \quad (\text{S6})$$

where $h_{l\theta/2}(\mathbf{k})$ is the kinetic term of the checkerboard lattice with a twist angle $l\theta/2$ from the x axis [$l = +1$ ($l = -1$) for the upper (lower) layer] and has the form of Eq.(1) in the main text. Let σ and τ represent the Pauli matrix for the sublattice degrees of freedom and the layer degrees of freedom respectively. The Hamiltonian with the moiré BZ as shown in Fig. 2(b) respects the following spatial symmetries.

$C_{2x/y}$ symmetry

$$C_{2x/y} f_{\mathbf{k}} C_{2x/y}^{-1} = \sigma_z f_{C_{2x/y} \mathbf{k}}, \quad [H, C_{2x/y}] = 0, \quad (\text{S7})$$

C_{4z} symmetry

$$C_{4z} f_{\mathbf{k}} C_{4z}^{-1} = \sigma_y f_{R_{\pi/2} \mathbf{k}}, \quad [H, C_{4z}] = 0, \quad (\text{S8})$$

The Hamiltonian also processes the particle-hole symmetry and time-reversal symmetry

Particle-hole symmetry

$$P f_{\mathbf{k}} P^{-1} = \sigma_y f_{-\mathbf{k}}, \quad PH(\mathbf{k})P^{-1} = -H^*(-\mathbf{k}), \quad (\text{S9})$$

Time reversal symmetry

$$T f_{\mathbf{k}} T^{-1} = f_{-\mathbf{k}}, \quad [H, T] = 0. \quad (\text{S10})$$

Notice that here the particle-hole symmetry is a rigorous one but will be broken when $w_{AA} \neq 0$ which is different from TBG. The system also preserves chiral symmetry if $w_{AA} = 0$ with the operator: $\sigma_y T$.

With these symmetries, we can fix the gauge of the wave function. We introduce the sewing matrix $B^g(\mathbf{k})$ for the C_{2z} , T and P symmetries.

$$[D(C_{2z})] u_n(\mathbf{k}) = \sum [B^{C_{2z}}(\mathbf{k})]_{m,n} u_m(-\mathbf{k}), \quad (\text{S11})$$

$$[D(T)] u_n(\mathbf{k}) = \sum [B^T(\mathbf{k})]_{m,n} u_m(-\mathbf{k}), \quad (\text{S12})$$

$$[D(P)] u_n(\mathbf{k}) = \sum [B^P(\mathbf{k})]_{m,n} u_m(-\mathbf{k}). \quad (\text{S13})$$

The sewing matrix can be simplified as

$$\begin{aligned} [B^{C_{2z}}(\mathbf{k})]_{m,n} &= \delta_{m,n} e^{i\varphi_n^{C_{2z}}(\mathbf{k})}, \\ [B^T(\mathbf{k})]_{m,n} &= \delta_{m,n} e^{i\varphi_n^T(\mathbf{k})}, \\ [B^P(\mathbf{k})]_{m,n} &= \delta_{-m,n} e^{i\varphi_n^P(\mathbf{k})}. \end{aligned} \quad (\text{S14})$$

These three symmetry operators can be combined to obtain two independent symmetry operations $C_{2z}P$ and $C_{2z}T$ which keep \mathbf{k} unchanged. The corresponding sewing matrices are defined by the following equations

$$\begin{aligned} [D(C_{2z})D(T)]u_n^*(\mathbf{k}) &= \sum_m [B^{C_{2z}T}(\mathbf{k})]_{m,n} u_m(\mathbf{k}), \\ [D(P)D(C_{2z})]u_n(\mathbf{k}) &= \sum_m [B^{C_{2z}P}(\mathbf{k})]_{m,n} u_m(\mathbf{k}). \end{aligned} \quad (\text{S15})$$

The symmetry operations $C_{2z}P$ and $C_{2z}T$ satisfy the properties

$$(C_{2z}T)^2 = (C_{2z}P)^2 = 1, \quad [C_{2z}T, C_{2z}P] = 1. \quad (\text{S16})$$

Thus we can adopt the following \mathbf{k} -independent sewing matrices

$$[B^{C_{2z}T}(\mathbf{k})]_{m,n} = \delta_{m,n}, \quad [B^{C_{2z}P}(\mathbf{k})]_{m,n} = -\text{sgn}(n)\delta_{-m,n}. \quad (\text{S17})$$

These sewing matrices can also be expressed by the Pauli matrix for the two flat bands

$$B^{C_{2z}T}(\mathbf{k}) = \zeta^0, \quad B^{C_{2z}P}(\mathbf{k}) = i\zeta^y, \quad (\text{S18})$$

where ζ represents the Pauli matrix for the two-flat-band subspace. We have chosen a similar form to the sewing matrix of the TBG systems adopted in Ref.[72], and the difference is that TBCB systems do not have two valleys. The wave function and thus the M matrix introduced in the main text and Appendix D,

$$M_{mn}(\mathbf{k}, \mathbf{q} + \mathbf{G}) = \sum_{\alpha, \mathbf{Q} \in \mathcal{Q}_{\pm}} u_{\mathbf{Q}-\mathbf{G}, \alpha, m}^*(\mathbf{k} + \mathbf{q}) u_{\mathbf{Q}, \alpha, n}(\mathbf{k}), \quad (\text{S19})$$

are also constrained by the two symmetries, $C_{2z}T$ and $C_{2z}P$, with the sewing matrices we obtained in Eq. (S18),

$$\begin{aligned} M_{mn}(\mathbf{k}, \mathbf{q} + \mathbf{G}) &= M_{mn}^*(\mathbf{k}, \mathbf{q} + \mathbf{G}), \\ M_{mn}(\mathbf{k}, \mathbf{q} + \mathbf{G}) &= [\zeta^y M(\mathbf{k}, \mathbf{q} + \mathbf{G}) \zeta^y]_{m,n}. \end{aligned} \quad (\text{S20})$$

Thus the M matrix takes the form

$$M(\mathbf{k}, \mathbf{q} + \mathbf{G}) = \zeta^0 \alpha_0(\mathbf{k}, \mathbf{q} + \mathbf{G}) + i\zeta^y \alpha_2(\mathbf{k}, \mathbf{q} + \mathbf{G}), \quad (\text{S21})$$

where $\alpha_0(\mathbf{k}, \mathbf{q} + \mathbf{G})$ and $\alpha_2(\mathbf{k}, \mathbf{q} + \mathbf{G})$ are real numbers. Besides, from the definition of the M matrix in the main text, the M matrix also satisfies the Hermiticity condition

$$M_{mn}^*(\mathbf{k}, \mathbf{q} + \mathbf{G}) = M_{nm}(\mathbf{k} + \mathbf{q}, -\mathbf{q} - \mathbf{G}), \quad (\text{S22})$$

which means that $\alpha_i(\mathbf{k}, \mathbf{q} + \mathbf{G})$ satisfy

$$\begin{aligned} \alpha_0(\mathbf{k}, \mathbf{q} + \mathbf{G}) &= \alpha_0(\mathbf{k} + \mathbf{q}, -\mathbf{q} - \mathbf{G}) \\ \alpha_2(\mathbf{k}, \mathbf{q} + \mathbf{G}) &= -\alpha_2(\mathbf{k} + \mathbf{q}, -\mathbf{q} - \mathbf{G}). \end{aligned} \quad (\text{S23})$$

We can also fix the relative gauge between the wave functions with momentum \mathbf{k} and those with momentum

$-\mathbf{k}$ by C_{2z} symmetry. Notice that in the TBCB system, C_{2z} , T , and P symmetries commute with each other, and we can choose the sewing matrix for these three symmetries

$$B^{C_{2z}}(\mathbf{k}) = \zeta^0, \quad B^T(\mathbf{k}) = \zeta^0, \quad B^P(\mathbf{k}) = i\zeta^y. \quad (\text{S24})$$

Thus, the M matrix also has the following constraint implied between the momentum \mathbf{k} and the momentum $-\mathbf{k}$:

$$M_{mn}(\mathbf{k}, \mathbf{q} + \mathbf{G}) = M_{mn}(-\mathbf{k}, -\mathbf{q} - \mathbf{G}), \quad (\text{S25})$$

which implies that

$$\alpha_a(\mathbf{k}, \mathbf{q} + \mathbf{G}) = \alpha_a(-\mathbf{k}, -\mathbf{q} - \mathbf{G}) \quad \text{for } a = 0, 2. \quad (\text{S26})$$

When the hopping $w_{AA} \neq 0$, the particle and chiral symmetries are broken, and Eq. (S20) no longer holds. Constrained by the real condition, the M matrix takes a more general form,

$$\begin{aligned} M(\mathbf{k}, \mathbf{q} + \mathbf{G}) &= \zeta^0 \alpha_0(\mathbf{k}, \mathbf{q} + \mathbf{G}) + \zeta^x \alpha_1(\mathbf{k}, \mathbf{q} + \mathbf{G}) \\ &\quad + i\zeta^y \alpha_2(\mathbf{k}, \mathbf{q} + \mathbf{G}) + \zeta^z \alpha_3(\mathbf{k}, \mathbf{q} + \mathbf{G}) \\ &= M_0(\mathbf{k}, \mathbf{q} + \mathbf{G}) + M_1(\mathbf{k}, \mathbf{q} + \mathbf{G}), \end{aligned} \quad (\text{S27})$$

where $\alpha_i(\mathbf{k}, \mathbf{q} + \mathbf{G})$ ($i = 0, 1, 2, 3$) are real numbers.

Similar to the chiral case introduced above, now $\alpha_i(\mathbf{k}, \mathbf{q} + \mathbf{G})$ are also constrained by the Hermiticity condition and the C_{2z} symmetry:

$$\begin{aligned} \alpha_a(\mathbf{k}, \mathbf{q} + \mathbf{G}) &= \alpha_a(\mathbf{k} + \mathbf{q}, -\mathbf{q} - \mathbf{G}) \quad \text{for } a = 0, 1, 3, \\ \alpha_2(\mathbf{k}, \mathbf{q} + \mathbf{G}) &= -\alpha_2(\mathbf{k} + \mathbf{q}, -\mathbf{q} - \mathbf{G}), \end{aligned} \quad (\text{S28})$$

$$\alpha_a(\mathbf{k}, \mathbf{q} + \mathbf{G}) = \alpha_a(-\mathbf{k}, -\mathbf{q} - \mathbf{G}), \quad \text{for } a = 0, 1, 2, 3. \quad (\text{S29})$$

Appendix D. Solving the Ground State of the Interacting Hamiltonian

The Coulomb interacting Hamiltonian of the system in the momentum space is written as

$$\mathcal{H} = \frac{1}{2A} \sum_{\mathbf{G} \in \mathcal{G}, \mathbf{q} \in \text{mBZ}} V(\mathbf{q} + \mathbf{G}) \delta \rho_{-\mathbf{q}-\mathbf{G}} \delta \rho_{\mathbf{q}+\mathbf{G}}, \quad (\text{S30})$$

where the gate Coulomb potential is $V(\mathbf{q}) = \pi d^2 U_d \frac{\tanh(d|\mathbf{q}|/2)}{d|\mathbf{q}|/2}$. Under the Chern band basis, the charge density term $\delta \rho_{-\mathbf{q}-\mathbf{G}}$ is

$$\delta \rho_{\mathbf{G}+\mathbf{q}} = \sum_{\mathbf{k}, s} \sum_{m, n} M_{m, n}(\mathbf{k}, \mathbf{q} + \mathbf{G}) \left(c_{m, s}^\dagger(\mathbf{k} + \mathbf{q}) c_{n, s}(\mathbf{k}) - \frac{1}{2} \delta_{\mathbf{q}, 0} \delta_{mn} \right), \quad (\text{S31})$$

where

$$M_{m,n}(\mathbf{k}, \mathbf{q} + \mathbf{G}) = \sum_{\alpha} \sum_{\mathbf{Q} \in \mathcal{Q}_{\pm}} u_{\mathbf{Q}-\mathbf{G}, \alpha, m}^*(\mathbf{k} + \mathbf{q}) u_{\mathbf{Q}, \alpha, n}(\mathbf{k}). \quad (\text{S32})$$

The interacting Hamiltonian now is written in a semi-

positive definite form

$$\mathcal{H} = \frac{1}{2\Omega_{\text{tot}}} \sum_{\mathbf{q} \in \text{mBZ}} \sum_{\mathbf{G} \in \mathcal{G}} O_{-\mathbf{q}, -\mathbf{G}} O_{\mathbf{q}, \mathbf{G}}, \quad (\text{S33})$$

where $O_{\mathbf{q}, \mathbf{G}} = \sum_{\mathbf{k}s} \sum_{m,n=\pm 1} \sqrt{V(\mathbf{q} + \mathbf{G})} M_{m,n}(\mathbf{k}, \mathbf{q} + \mathbf{G}) (c_{m,s}^{\dagger}(\mathbf{k} + \mathbf{q}) c_{n,s}(\mathbf{k}) - \frac{1}{2} \delta_{\mathbf{q},0} \delta_{m,n})$.

Notice that the number of the electron N is conserved; thus we are able to introduce a Lagrange multiplier $A_{\mathbf{G}}$

$$\mathcal{H} = \frac{1}{2\Omega_{\text{tot}}} \sum_{\mathbf{G} \in \mathcal{G}} \left[\left(\sum_{\mathbf{q}} (O_{\mathbf{q}, \mathbf{G}} - A_{\mathbf{G}} N \delta_{\mathbf{q},0}) (O_{-\mathbf{q}, -\mathbf{G}} - A_{-\mathbf{G}} N \delta_{-\mathbf{q},0}) \right) + 2A_{-\mathbf{G}} N O_{0,\mathbf{G}} - A_{-\mathbf{G}} A_{\mathbf{G}} N^2 \right]. \quad (\text{S34})$$

When the flat metric condition [72, 73] $M_{m,n}(\mathbf{k}, \mathbf{G}) = \xi(\mathbf{G}) \delta_{m,n}$ is satisfied or filling factor $\nu = 0$, the last two terms in Eq. (S34) are constant which depend on N . In this way, one can easily conclude that the ground state of the interacting Hamiltonian satisfies the equation

$$(O_{\mathbf{q}, \mathbf{G}} - A_{\mathbf{G}} N \delta_{\mathbf{q},0}) |\Psi\rangle = 0. \quad (\text{S35})$$

To solve the ground state, one only needs to solve Eq. (S35). In general, the Flat Metric Condition is not strictly satisfied except for $\mathbf{G} = \mathbf{0}$. Fortunately, when the flat metric condition is not largely violated, the ground states which satisfy Eq. (S35) persist as long as the gap between the ground states and exciting states is not closed. Since the wave function decreases exponentially as \mathbf{G} increases for the moiré Hamiltonian[28], one can assume that the flat metric condition is not largely violated and the ground state derived above is the real ground state of the system. Future studies can adopt the real-space projection method [50, 122] to confirm our conclusion for ground states.

* heailei@yzu.edu.cn

† yaohong@tsinghua.edu.cn

- [1] Y. Cao, V. Fatemi, A. Demir, S. Fang, S. L. Tomarken, J. Y. Luo, J. D. Sanchez-Yamagishi, K. Watanabe, T. Taniguchi, E. Kaxiras, R. C. Ashoori, and P. Jarillo-Herrero, Correlated insulator behaviour at half-filling in magic-angle graphene superlattices, *Nature* **556**, 80 (2018).
- [2] Y. Cao, V. Fatemi, S. Fang, K. Watanabe, T. Taniguchi, E. Kaxiras, and P. Jarillo-Herrero, Unconventional superconductivity in magic-angle graphene superlattices, *Nature* **556**, 43 (2018).
- [3] A. Kerelsky, L. J. McGilly, D. M. Kennes, L. Xian, M. Yankowitz, S. Chen, K. Watanabe, T. Taniguchi, J. Hone, C. Dean, A. Rubio, and A. N. Pasupathy, Maximized electron interactions at the magic angle in twisted bilayer graphene, *Nature* **572**, 95 (2019).

- [4] Y. Xie, B. Lian, B. Jäck, X. Liu, C.-L. Chiu, K. Watanabe, T. Taniguchi, B. A. Bernevig, and A. Yazdani, Spectroscopic signatures of many-body correlations in magic-angle twisted bilayer graphene, *Nature* **572**, 101 (2019).
- [5] A. L. Sharpe, E. J. Fox, A. W. Barnard, J. Finney, K. Watanabe, T. Taniguchi, M. A. Kastner, and D. Goldhaber-Gordon, Emergent ferromagnetism near three-quarters filling in twisted bilayer graphene, *Science* **365**, 605–608 (2019).
- [6] Y. Jiang, X. Lai, K. Watanabe, T. Taniguchi, K. Haule, J. Mao, and E. Y. Andrei, Charge order and broken rotational symmetry in magic-angle twisted bilayer graphene, *Nature* **573**, 91 (2019).
- [7] M. Serlin, C. L. Tschirhart, H. Polshyn, Y. Zhang, J. Zhu, K. Watanabe, T. Taniguchi, L. Balents, and A. F. Young, Intrinsic quantized anomalous hall effect in a moiré heterostructure, *Science* **367**, 900 (2020), <https://www.science.org/doi/pdf/10.1126/science.aay5533>.
- [8] Y. Choi, J. Kemmer, Y. Peng, A. Thomson, H. Arora, R. Polski, Y. Zhang, H. Ren, J. Alicea, G. Refael, F. von Oppen, K. Watanabe, T. Taniguchi, and S. Nadj-Perge, Electronic correlations in twisted bilayer graphene near the magic angle, *Nature Physics* **15**, 1174 (2019).
- [9] X. Lu, P. Stepanov, W. Yang, M. Xie, M. A. Aamir, I. Das, C. Urgell, K. Watanabe, T. Taniguchi, G. Zhang, and et al., Superconductors, orbital magnets and correlated states in magic-angle bilayer graphene, *Nature* **574**, 653–657 (2019).
- [10] M. Yankowitz, S. Chen, H. Polshyn, Y. Zhang, K. Watanabe, T. Taniguchi, D. Graf, A. F. Young, and C. R. Dean, Tuning superconductivity in twisted bilayer graphene, *Science* **363**, 1059–1064 (2019).
- [11] Y. Cao, D. Chowdhury, D. Rodan-Legrain, O. Rubies-Bigorda, K. Watanabe, T. Taniguchi, T. Senthil, and P. Jarillo-Herrero, Strange metal in magic-angle graphene with near planckian dissipation, *Phys. Rev. Lett.* **124**, 076801 (2020).
- [12] Y. Choi, H. Kim, Y. Peng, A. Thomson, C. Lewandowski, R. Polski, Y. Zhang, H. S. Arora, K. Watanabe, T. Taniguchi, J. Alicea, and S. Nadj-Perge, Tracing out correlated chern insulators in magic angle twisted bilayer graphene (2020), arXiv:2008.11746 [cond-mat.str-el].

- [13] D. Wong, K. Nuckolls, M. Oh, B. Lian, Y. Xie, S. Jeon, K. Watanabe, T. Taniguchi, B. Bernevig, and A. Yazdani, Cascade of electronic transitions in magic-angle twisted bilayer graphene, *Nature* **582**, 198 (2020).
- [14] U. Zondiner, A. Rozen, D. Rodan-Legrain, Y. Cao, R. Queiroz, T. Taniguchi, K. Watanabe, Y. Oreg, F. von Oppen, A. Stern, E. Berg, P. Jarillo-Herrero, and S. Ilani, Cascade of phase transitions and dirac revivals in magic-angle graphene, *Nature* **582**, 203 (2020).
- [15] Y. Saito, J. Ge, K. Watanabe, T. Taniguchi, and A. F. Young, Independent superconductors and correlated insulators in twisted bilayer graphene, *Nature Physics* **16**, 926 (2020).
- [16] P. Stepanov, I. Das, X. Lu, A. Fahimniya, K. Watanabe, T. Taniguchi, F. H. L. Koppens, J. Lischner, L. Levitov, and D. K. Efetov, Untying the insulating and superconducting orders in magic-angle graphene, *Nature* **583**, 375 (2020).
- [17] H. S. Arora, R. Polski, Y. Zhang, A. Thomson, Y. Choi, H. Kim, Z. Lin, I. Z. Wilson, X. Xu, J.-H. Chu, K. Watanabe, T. Taniguchi, J. Alicea, and S. Nadj-Perge, Superconductivity in metallic twisted bilayer graphene stabilized by wse₂, *Nature* **583**, 379 (2020).
- [18] K. P. Nuckolls, M. Oh, D. Wong, B. Lian, K. Watanabe, T. Taniguchi, B. A. Bernevig, and A. Yazdani, Strongly correlated chern insulators in magic-angle twisted bilayer graphene, *Nature* **588**, 610 (2020).
- [19] Y. Saito, J. Ge, L. Rademaker, K. Watanabe, T. Taniguchi, D. A. Abanin, and A. F. Young, Hofstadter subband ferromagnetism and symmetry-broken chern insulators in twisted bilayer graphene, *Nature Physics* **17**, 478–481 (2021).
- [20] X. Liu, Z. Wang, K. Watanabe, T. Taniguchi, O. Vafeek, and J. I. A. Li, Tuning electron correlation in magic-angle twisted bilayer graphene using coulomb screening, *Science* **371**, 1261–1265 (2021).
- [21] S. Wu, Z. Zhang, K. Watanabe, T. Taniguchi, and E. Y. Andrei, Chern insulators, van hove singularities and topological flat bands in magic-angle twisted bilayer graphene, *Nature Materials* **20**, 488–494 (2021).
- [22] I. Das, X. Lu, J. Herzog-Arbeitman, Z.-D. Song, K. Watanabe, T. Taniguchi, B. A. Bernevig, and D. K. Efetov, Symmetry-broken chern insulators and rashba-like landau-level crossings in magic-angle bilayer graphene, *Nature Physics* **17**, 710–714 (2021).
- [23] J. M. Park, Y. Cao, K. Watanabe, T. Taniguchi, and P. Jarillo-Herrero, Flavour hund’s coupling, chern gaps and charge diffusivity in moiré graphene, *Nature* **592**, 43–48 (2021).
- [24] A. Rozen, J. M. Park, U. Zondiner, Y. Cao, D. Rodan-Legrain, T. Taniguchi, K. Watanabe, Y. Oreg, A. Stern, E. Berg, and et al., Entropic evidence for a pomeranchuk effect in magic-angle graphene, *Nature* **592**, 214–219 (2021).
- [25] X. Lu, B. Lian, G. Chaudhary, B. A. Piot, G. Romagnoli, K. Watanabe, T. Taniguchi, M. Poggio, A. H. MacDonald, B. A. Bernevig, and D. K. Efetov, Multiple flat bands and topological hofstadter butterfly in twisted bilayer graphene close to the second magic angle (2020), arXiv:2006.13963 [cond-mat.mes-hall].
- [26] Y. Xie, A. T. Pierce, J. M. Park, D. E. Parker, E. Khalaf, P. Ledwith, Y. Cao, S. H. Lee, S. Chen, P. R. Forrester, K. Watanabe, T. Taniguchi, A. Vishwanath, P. Jarillo-Herrero, and A. Yacoby, Fractional chern insulators in magic-angle twisted bilayer graphene (2021), arXiv:2107.10854 [cond-mat.mes-hall].
- [27] R. Bistritzer and A. H. MacDonald, Moiré bands in twisted double-layer graphene, *Proceedings of the National Academy of Sciences* **108**, 12233 (2011), <https://www.pnas.org/content/108/30/12233.full.pdf>.
- [28] B. A. Bernevig, Z.-D. Song, N. Regnault, and B. Lian, Twisted bilayer graphene. i. matrix elements, approximations, perturbation theory, and a $k \cdot p$ two-band model, *Phys. Rev. B* **103**, 205411 (2021).
- [29] Z. Song, Z. Wang, W. Shi, G. Li, C. Fang, and B. A. Bernevig, All magic angles in twisted bilayer graphene are topological, *Phys. Rev. Lett.* **123**, 036401 (2019).
- [30] H. C. Po, L. Zou, T. Senthil, and A. Vishwanath, Faithful tight-binding models and fragile topology of magic-angle bilayer graphene, *Phys. Rev. B* **99**, 195455 (2019).
- [31] J. Ahn, S. Park, and B.-J. Yang, Failure of nielsen-ninomiya theorem and fragile topology in two-dimensional systems with space-time inversion symmetry: Application to twisted bilayer graphene at magic angle, *Phys. Rev. X* **9**, 021013 (2019).
- [32] Z.-D. Song, B. Lian, N. Regnault, and B. A. Bernevig, Twisted bilayer graphene. ii. stable symmetry anomaly, *Phys. Rev. B* **103**, 205412 (2021).
- [33] C. Xu and L. Balents, Topological superconductivity in twisted multilayer graphene, *Phys. Rev. Lett.* **121**, 087001 (2018).
- [34] C.-C. Liu, L.-D. Zhang, W.-Q. Chen, and F. Yang, Chiral spin density wave and $d+id$ superconductivity in the magic-angle-twisted bilayer graphene, *Phys. Rev. Lett.* **121**, 217001 (2018).
- [35] F. Wu, A. H. MacDonald, and I. Martin, Theory of phonon-mediated superconductivity in twisted bilayer graphene, *Phys. Rev. Lett.* **121**, 257001 (2018).
- [36] M. Koshino, N. F. Q. Yuan, T. Koretsune, M. Ochi, K. Kuroki, and L. Fu, Maximally localized wannier orbitals and the extended hubbard model for twisted bilayer graphene, *Phys. Rev. X* **8**, 031087 (2018).
- [37] H. C. Po, L. Zou, A. Vishwanath, and T. Senthil, Origin of mott insulating behavior and superconductivity in twisted bilayer graphene, *Phys. Rev. X* **8**, 031089 (2018).
- [38] H. Isobe, N. F. Q. Yuan, and L. Fu, Unconventional superconductivity and density waves in twisted bilayer graphene, *Phys. Rev. X* **8**, 041041 (2018).
- [39] H. Guo, X. Zhu, S. Feng, and R. T. Scalettar, Pairing symmetry of interacting fermions on a twisted bilayer graphene superlattice, *Phys. Rev. B* **97**, 235453 (2018).
- [40] A. Thomson, S. Chatterjee, S. Sachdev, and M. S. Scheurer, Triangular antiferromagnetism on the honeycomb lattice of twisted bilayer graphene, *Phys. Rev. B* **98**, 075109 (2018).
- [41] J. F. Dodaro, S. A. Kivelson, Y. Schattner, X. Q. Sun, and C. Wang, Phases of a phenomenological model of twisted bilayer graphene, *Phys. Rev. B* **98**, 075154 (2018).
- [42] M. Ochi, M. Koshino, and K. Kuroki, Possible correlated insulating states in magic-angle twisted bilayer graphene under strongly competing interactions, *Phys. Rev. B* **98**, 081102 (2018).
- [43] X. Y. Xu, K. T. Law, and P. A. Lee, Kekulé valence bond order in an extended hubbard model on the honeycomb lattice with possible applications to twisted bilayer graphene, *Phys. Rev. B* **98**, 121406 (2018).

- [44] F. Guinea and N. R. Walet, Electrostatic effects, band distortions, and superconductivity in twisted graphene bilayers, *Proceedings of the National Academy of Sciences* **115**, 13174 (2018), <https://www.pnas.org/content/115/52/13174.full.pdf>.
- [45] D. M. Kennes, J. Lischner, and C. Karrasch, Strong correlations and $d + id$ superconductivity in twisted bilayer graphene, *Phys. Rev. B* **98**, 241407 (2018).
- [46] J. W. F. Venderbos and R. M. Fernandes, Correlations and electronic order in a two-orbital honeycomb lattice model for twisted bilayer graphene, *Phys. Rev. B* **98**, 245103 (2018).
- [47] Y.-Z. You and A. Vishwanath, Superconductivity from valley fluctuations and approximate $so(4)$ symmetry in a weak coupling theory of twisted bilayer graphene, *npj Quantum Materials* **4**, 16 (2019).
- [48] B. Roy and V. Juričić, Unconventional superconductivity in nearly flat bands in twisted bilayer graphene, *Phys. Rev. B* **99**, 121407 (2019).
- [49] J. González and T. Stauber, Kohn-luttinger superconductivity in twisted bilayer graphene, *Phys. Rev. Lett.* **122**, 026801 (2019).
- [50] J. Kang and O. Vafek, Strong coupling phases of partially filled twisted bilayer graphene narrow bands, *Phys. Rev. Lett.* **122**, 246401 (2019).
- [51] K. Seo, V. N. Kotov, and B. Uchoa, Ferromagnetic mott state in twisted graphene bilayers at the magic angle, *Phys. Rev. Lett.* **122**, 246402 (2019).
- [52] B. Lian, Z. Wang, and B. A. Bernevig, Twisted bilayer graphene: A phonon-driven superconductor, *Phys. Rev. Lett.* **122**, 257002 (2019).
- [53] Y. Da Liao, Z. Y. Meng, and X. Y. Xu, Valence bond orders at charge neutrality in a possible two-orbital extended hubbard model for twisted bilayer graphene, *Phys. Rev. Lett.* **123**, 157601 (2019).
- [54] G. W. Burg, J. Zhu, T. Taniguchi, K. Watanabe, A. H. MacDonald, and E. Tutuc, Correlated insulating states in twisted double bilayer graphene, *Phys. Rev. Lett.* **123**, 197702 (2019).
- [55] X. Hu, T. Hyart, D. I. Pikulin, and E. Rossi, Geometric and conventional contribution to the superfluid weight in twisted bilayer graphene, *Phys. Rev. Lett.* **123**, 237002 (2019).
- [56] T. Huang, L. Zhang, and T. Ma, Antiferromagnetically ordered mott insulator and $d + id$ superconductivity in twisted bilayer graphene: a quantum monte carlo study, *Science Bulletin* **64**, 310 (2019).
- [57] F. Wu and S. Das Sarma, Collective excitations of quantum anomalous hall ferromagnets in twisted bilayer graphene, *Phys. Rev. Lett.* **124**, 046403 (2020).
- [58] M. Xie and A. H. MacDonald, Nature of the correlated insulator states in twisted bilayer graphene, *Phys. Rev. Lett.* **124**, 097601 (2020).
- [59] N. Bultinck, S. Chatterjee, and M. P. Zaletel, Mechanism for anomalous hall ferromagnetism in twisted bilayer graphene, *Phys. Rev. Lett.* **124**, 166601 (2020).
- [60] F. Xie, Z. Song, B. Lian, and B. A. Bernevig, Topology-bounded superfluid weight in twisted bilayer graphene, *Phys. Rev. Lett.* **124**, 167002 (2020).
- [61] C. Repellin, Z. Dong, Y.-H. Zhang, and T. Senthil, Ferromagnetism in narrow bands of moiré superlattices, *Phys. Rev. Lett.* **124**, 187601 (2020).
- [62] P. J. Ledwith, G. Tarnopolsky, E. Khalaf, and A. Vishwanath, Fractional chern insulator states in twisted bilayer graphene: An analytical approach, *Phys. Rev. Research* **2**, 023237 (2020).
- [63] C. Repellin and T. Senthil, Chern bands of twisted bilayer graphene: Fractional chern insulators and spin phase transition, *Phys. Rev. Research* **2**, 023238 (2020).
- [64] A. Julku, T. J. Peltonen, L. Liang, T. T. Heikkilä, and P. Törmä, Superfluid weight and berezinskii-kosterlitz-thouless transition temperature of twisted bilayer graphene, *Phys. Rev. B* **101**, 060505 (2020).
- [65] T. Soejima, D. E. Parker, N. Bultinck, J. Hauschild, and M. P. Zaletel, Efficient simulation of moiré materials using the density matrix renormalization group, *Phys. Rev. B* **102**, 205111 (2020).
- [66] Y. Zhang, K. Jiang, Z. Wang, and F. Zhang, Correlated insulating phases of twisted bilayer graphene at commensurate filling fractions: A hartree-fock study, *Phys. Rev. B* **102**, 035136 (2020).
- [67] O. Vafek and J. Kang, Renormalization group study of hidden symmetry in twisted bilayer graphene with coulomb interactions, *Phys. Rev. Lett.* **125**, 257602 (2020).
- [68] N. Bultinck, E. Khalaf, S. Liu, S. Chatterjee, A. Vishwanath, and M. P. Zaletel, Ground state and hidden symmetry of magic-angle graphene at even integer filling, *Phys. Rev. X* **10**, 031034 (2020).
- [69] M. Christos, S. Sachdev, and M. S. Scheurer, Superconductivity, correlated insulators, and wess-zumino-witten terms in twisted bilayer graphene, *Proceedings of the National Academy of Sciences* **117**, 29543 (2020), <https://www.pnas.org/content/117/47/29543.full.pdf>.
- [70] Y. Da Liao, J. Kang, C. N. Breiø, X. Y. Xu, H.-Q. Wu, B. M. Andersen, R. M. Fernandes, and Z. Y. Meng, Correlation-induced insulating topological phases at charge neutrality in twisted bilayer graphene, *Phys. Rev. X* **11**, 011014 (2021).
- [71] J. Liu and X. Dai, Theories for the correlated insulating states and quantum anomalous hall effect phenomena in twisted bilayer graphene, *Phys. Rev. B* **103**, 035427 (2021).
- [72] B. A. Bernevig, Z.-D. Song, N. Regnault, and B. Lian, Twisted bilayer graphene. iii. interacting hamiltonian and exact symmetries, *Phys. Rev. B* **103**, 205413 (2021).
- [73] B. Lian, Z.-D. Song, N. Regnault, D. K. Efetov, A. Yazdani, and B. A. Bernevig, Twisted bilayer graphene. iv. exact insulator ground states and phase diagram, *Phys. Rev. B* **103**, 205414 (2021).
- [74] B. A. Bernevig, B. Lian, A. Cowsik, F. Xie, N. Regnault, and Z.-D. Song, Twisted bilayer graphene. v. exact analytic many-body excitations in coulomb hamiltonians: Charge gap, goldstone modes, and absence of cooper pairing, *Phys. Rev. B* **103**, 205415 (2021).
- [75] F. Xie, A. Cowsik, Z.-D. Song, B. Lian, B. A. Bernevig, and N. Regnault, Twisted bilayer graphene. vi. an exact diagonalization study at nonzero integer filling, *Phys. Rev. B* **103**, 205416 (2021).
- [76] S. Liu, E. Khalaf, J. Y. Lee, and A. Vishwanath, Nematic topological semimetal and insulator in magic-angle bilayer graphene at charge neutrality, *Phys. Rev. Research* **3**, 013033 (2021).
- [77] K. Hejazi, X. Chen, and L. Balents, Hybrid wannier chern bands in magic angle twisted bilayer graphene and the quantized anomalous hall effect, *Phys. Rev. Research* **3**, 013242 (2021).

- [78] E. Khalaf, S. Chatterjee, N. Bultinck, M. P. Zaletel, and A. Vishwanath, Charged skyrmions and topological origin of superconductivity in magic-angle graphene, *Science Advances* **7**, eabf5299 (2021).
- [79] C. Lewandowski, D. Chowdhury, and J. Ruhman, Pairing in magic-angle twisted bilayer graphene: Role of phonon and plasmon umklapp, *Phys. Rev. B* **103**, 235401 (2021).
- [80] J. Wang, J. Cano, A. J. Millis, Z. Liu, and B. Yang, Exact Landau level description of geometry and interaction in a flatband (2021), arXiv:2105.07491 [cond-mat.mes-hall].
- [81] F. Wu, T. Lovorn, E. Tutuc, and A. H. MacDonald, Hubbard model physics in transition metal dichalcogenide moiré bands, *Phys. Rev. Lett.* **121**, 026402 (2018).
- [82] F. Wu, T. Lovorn, E. Tutuc, I. Martin, and A. H. MacDonald, Topological insulators in twisted transition metal dichalcogenide homobilayers, *Phys. Rev. Lett.* **122**, 086402 (2019).
- [83] Y. Tang, L. Li, T. Li, Y. Xu, S. Liu, K. Barmak, K. Watanabe, T. Taniguchi, A. H. MacDonald, J. Shan, and K. F. Mak, Simulation of Hubbard model physics in wse_2/ws_2 moiré superlattices, *Nature* **579**, 353 (2020).
- [84] E. C. Regan, D. Wang, C. Jin, M. I. Bakti Utama, B. Gao, X. Wei, S. Zhao, W. Zhao, Z. Zhang, K. Yumigeta, M. Blei, J. D. Carlström, K. Watanabe, T. Taniguchi, S. Tongay, M. Crommie, A. Zettl, and F. Wang, Mott and generalized Wigner crystal states in wse_2/ws_2 moiré superlattices, *Nature* **579**, 359 (2020).
- [85] H. Pan, F. Wu, and S. Das Sarma, Quantum phase diagram of a moiré-Hubbard model, *Phys. Rev. B* **102**, 201104 (2020).
- [86] S. Shabani, D. Halbertal, W. Wu, M. Chen, S. Liu, J. Hone, W. Yao, D. N. Basov, X. Zhu, and A. N. Pasupathy, Deep moiré potentials in twisted transition metal dichalcogenide bilayers, *Nature Physics* **17**, 720 (2021).
- [87] Y. Zhang, T. Liu, and L. Fu, Electronic structures, charge transfer, and charge order in twisted transition metal dichalcogenide bilayers, *Phys. Rev. B* **103**, 155142 (2021).
- [88] Y. Xu, S. Liu, D. A. Rhodes, K. Watanabe, T. Taniguchi, J. Hone, V. Elser, K. F. Mak, and J. Shan, Correlated insulating states at fractional fillings of moiré superlattices, *Nature* **587**, 214 (2020).
- [89] Z. Bi and L. Fu, Excitonic density wave and spin-valley superfluid in bilayer transition metal dichalcogenide, *Nature Communications* **12**, 642 (2021).
- [90] N. Morales-Durán, A. H. MacDonald, and P. Potasz, Metal-insulator transition in transition metal dichalcogenide heterobilayer moiré superlattices, *Phys. Rev. B* **103**, L241110 (2021).
- [91] J. Zang, J. Wang, J. Cano, and A. J. Millis, Hartree-Fock study of the moiré Hubbard model for twisted bilayer transition metal dichalcogenides, *Phys. Rev. B* **104**, 075150 (2021).
- [92] Z. Zhang, Y. Wang, K. Watanabe, T. Taniguchi, K. Ueno, E. Tutuc, and B. J. LeRoy, Flat bands in twisted bilayer transition metal dichalcogenides, *Nature Physics* **16**, 1093 (2020).
- [93] T. Li, S. Jiang, B. Shen, Y. Zhang, L. Li, T. Devakul, K. Watanabe, T. Taniguchi, L. Fu, J. Shan, and K. F. Mak, Quantum anomalous Hall effect from intertwined moiré bands (2021), arXiv:2107.01796 [cond-mat.mes-hall].
- [94] T. Devakul, V. Crépel, Y. Zhang, and L. Fu, Magic in twisted transition metal dichalcogenide bilayers (2021), arXiv:2106.11954 [cond-mat.mes-hall].
- [95] T. Devakul and L. Fu, Quantum anomalous Hall effect from inverted charge transfer gap (2021), arXiv:2109.13909 [cond-mat.str-el].
- [96] D. Kiese, Y. He, C. Hickey, A. Rubio, and D. M. Kennes, TMDs as a platform for spin liquid physics: A strong coupling study of twisted bilayer wse_2 (2021), arXiv:2110.10179 [cond-mat.str-el].
- [97] K. Sun, H. Yao, E. Fradkin, and S. A. Kivelson, Topological insulators and nematic phases from spontaneous symmetry breaking in 2d Fermi systems with a quadratic band crossing, *Phys. Rev. Lett.* **103**, 046811 (2009).
- [98] O. Vafek and K. Yang, Many-body instability of Coulomb interacting bilayer graphene: Renormalization group approach, *Phys. Rev. B* **81**, 041401 (2010).
- [99] F. Zhang, H. Min, M. Polini, and A. H. MacDonald, Spontaneous inversion symmetry breaking in graphene bilayers, *Phys. Rev. B* **81**, 041402 (2010).
- [100] Y. You and E. Fradkin, Field theory of nematicity in the spontaneous quantum anomalous Hall effect, *Phys. Rev. B* **88**, 235124 (2013).
- [101] T. Neupert, L. Santos, C. Chamon, and C. Mudry, Fractional quantum Hall states at zero magnetic field, *Phys. Rev. Lett.* **106**, 236804 (2011).
- [102] X.-L. Qi, Generic wave-function description of fractional quantum anomalous Hall states and fractional topological insulators, *Phys. Rev. Lett.* **107**, 126803 (2011).
- [103] F. Wang and Y. Ran, Nearly flat band with Chern number $c = 2$ on the dice lattice, *Phys. Rev. B* **84**, 241103 (2011).
- [104] Y.-F. Wang, H. Yao, C.-D. Gong, and D. N. Sheng, Fractional quantum Hall effect in topological flat bands with Chern number two, *Phys. Rev. B* **86**, 201101 (2012).
- [105] S. Yang, Z.-C. Gu, K. Sun, and S. Das Sarma, Topological flat band models with arbitrary Chern numbers, *Phys. Rev. B* **86**, 241112 (2012).
- [106] Y.-L. Wu, N. Regnault, and B. A. Bernevig, Bloch model wave functions and pseudopotentials for all fractional Chern insulators, *Phys. Rev. Lett.* **110**, 106802 (2013).
- [107] B. Andrews and A. Soluyanov, Fractional quantum Hall states for moiré superstructures in the Hofstadter regime, *Phys. Rev. B* **101**, 235312 (2020).
- [108] Z. Liu, A. Abouelkomsan, and E. J. Bergholtz, Gate-tunable fractional Chern insulators in twisted double bilayer graphene, *Phys. Rev. Lett.* **126**, 026801 (2021).
- [109] B. Andrews, T. Neupert, and G. Möller, Stability, phase transitions, and numerical breakdown of fractional Chern insulators in higher Chern bands of the Hofstadter model, *Phys. Rev. B* **104**, 125107 (2021).
- [110] A. H. Castro Neto, F. Guinea, N. M. R. Peres, K. S. Novoselov, and A. K. Geim, The electronic properties of graphene, *Rev. Mod. Phys.* **81**, 109 (2009).
- [111] C.-Z. Chang, J. Zhang, X. Feng, J. Shen, Z. Zhang, M. Guo, K. Li, Y. Ou, P. Wei, L.-L. Wang, Z.-Q. Ji, Y. Feng, S. Ji, X. Chen, J. Jia, X. Dai, Z. Fang, S.-C. Zhang, K. He, Y. Wang, L. Lu, X.-C. Ma, and Q.-K. Xue, Experimental observation of the quantum anomalous Hall effect in a magnetic topological insulator, *Science* **340**, 167 (2013), <https://www.science.org/doi/pdf/10.1126/science.1234414>.

- [112] Notice that we've adopted the real gauge such that the $d_i(\mathbf{k})$ are real, in this case the Hamiltonian is not periodic and satisfies $H(\mathbf{k} + \mathbf{G}_i) = \sigma_z H(\mathbf{k}) \sigma_z$, where \mathbf{G}_i is the reciprocal vector of the lattice[31]. We can also choose a periodic and complex gauge and in this case we have $d_x(\mathbf{k}) - id_y(\mathbf{k}) = -\left(1 + e^{-ik_x} + e^{-ik_y} + e^{-i(k_x+k_y)}\right)$.
- [113] Note that $T_{1,2} = w_A A \sigma_0 \pm w_{AB} \sigma_x$, which commute with the unitary transformation $U = e^{i\frac{\pi}{2}\sigma_x}$, such that the tunneling matrix is not changed by the unitary transformation.
- [114] G. Tarnopolsky, A. J. Kruchkov, and A. Vishwanath, Origin of magic angles in twisted bilayer graphene, Phys. Rev. Lett. **122**, 106405 (2019).
- [115] A. Alexandradinata, Z. Wang, and B. A. Bernevig, Topological insulators from group cohomology, Phys. Rev. X **6**, 021008 (2016).
- [116] High-Chern number flat bands can also be realized in twisted graphene multilayers [120, 121].
- [117] G. Wirth, M. Ölschläger, and A. Hemmerich, Evidence for orbital superfluidity in the p-band of a bipartite optical square lattice, Nature Physics **7**, 147 (2011).
- [118] K. Sun, W. V. Liu, A. Hemmerich, and S. Das Sarma, Topological semimetal in a fermionic optical lattice, Nature Physics **8**, 67 (2012).
- [119] A. González-Tudela and J. I. Cirac, Cold atoms in twisted-bilayer optical potentials, Phys. Rev. A **100**, 053604 (2019).
- [120] P. J. Ledwith, A. Vishwanath, and E. Khalaf, A family of ideal chern flat bands with arbitrary chern number in chiral twisted graphene multilayers (2021), arXiv:2109.11514 [cond-mat.str-el].
- [121] Jie Wang and Zhao Liu, Hierarchy of Ideal Flatbands in Chiral Twisted Multilayer Graphene Models, Phys. Rev. Lett. **128**, 176403 (2022).
- [122] J. Kang and O. Vafek, Symmetry, Maximally Localized Wannier States, and a Low-Energy Model for Twisted Bilayer Graphene Narrow Bands, Phys. Rev. X. **8**, 031088 (2018).